





Impact of mesh quality on the numerical estimation of saturated water conductivity of pore media**

Bartłomiej Gackiewicz¹^{*}, Krzysztof Lamorski¹, Cezary Sławiński¹, Shao-Yiu Hsu²,
and Liang-Cheng Chang³

¹Institute of Agrophysics, Polish Academy of Sciences, Doświadczalna 4, 20-290 Lublin, Poland

²Department of Bioenvironmental Systems Engineering, National Taiwan University, Taipei 10617, Taiwan

³Department of Civil Engineering, National Chiao Tung University, 1001 University Road, Hsinchu, Taiwan

Received September 25, 2020; accepted November 10, 2020

Abstract. The numerical modelling of transport phenomena in porous media often requires a compromise between grid precision and the accuracy of simulation results. This study demonstrates the impact of errors on the accuracy of the reproduction of the actual pore space by the numerical grid on the estimated values of the saturated water conductivity. Four types of computational grids with varying levels of complexity were prepared for each of the 12 tomographic images of the porous specimens. The specific surfaces and total porosities were calculated for each of the meshes and compared with those parameters calculated for binarized tomographic images. Simulations of steady flow were performed on the computational grids, and the saturated water conductivity values were calculated. It has been shown that an insufficiently accurate mesh only reproduces the largest pore spaces in the analysed sample, which most often leads to an underestimation of the water conductivity coefficient. The following criterion for the optimal accuracy of the computational grid is proposed, it is based on the voxel size of the tomographic images of the porous media: the minimum size of the cell in the mesh used for simulations has to be at most two times the size of the voxel used in the tomographic scans of the porous medium.

Keywords: porous media, numerical modelling, hydraulic conductivity, mesh accuracy

INTRODUCTION

An increase in computing capabilities has made it possible to directly model transport processes in porous media. Water flow in soils (Dal Ferro *et al.*, 2015; Khan *et al.*, 2012; Larsbo *et al.*, 2014) hydraulic properties and state variables and measures of preferential transport. Experiments were carried out under near-saturated conditions on undisturbed columns sampled from four agricultural topsoils of contrasting texture and structure. Macropore network characteristics were computed from 3-D X-ray tomography images of the soil pore system. Non-reactive solute transport experiments were carried out at five steady-state water flow rates from 2 to 12 mm h⁻¹. The degree of preferential transport was evaluated by the normalised 5% solute arrival time and the apparent dispersivity calculated from the resulting breakthrough curves. Near-saturated hydraulic conductivities were measured on the same samples using a tension disc infiltrometer placed on top of the columns. Results showed that many of the macropore network characteristics were inter-correlated. For example, large macroporosities were associated with larger specific macropore surface areas and better local connectivity of the macropore network. Generally, an increased flow rate resulted in earlier solute breakthrough and a shifting of

*Corresponding author e-mail: bgackiewicz@ipan.lublin.pl

**This work was partially supported by a grant from the Polish National Centre for Research and Development, contract No. PL-TW/IV/5/2017, and the Taiwanese Ministry of Science and Technology: MOST-106-2923-E-009-001-MY3.

the arrival of peak concentration towards smaller drained volumes. Columns with smaller macroporosities, poorer local connectivity of the macropore network and smaller near-saturated hydraulic conductivities exhibited a greater degree of preferential transport. This can be explained by the fact that, with only two exceptions, global (*i.e.* sample scale, rocks (Andrä *et al.*, 2013) and other porous media is a simulated phenomenon belonging to a broader class of transport processes, which also includes transport of: heat (Chen *et al.*, 2017), gases (Zuo *et al.*, 2017) and chemical compounds (Jarvis, 2007) fissures and interaggregate voids as well as multiphase transport (Horgue *et al.*, 2015).

Saturated water conductivity is one of basic macroscopic hydrological characteristics of porous media. It is determined by soil water flow processes occurring at the microscale. There are well-established techniques for the direct modelling of saturated water conductivity (SWC) in geological porous media based on X-ray computational tomography (CT) imaging and the Navier-Stokes (NS) equations, where the transport processes are simulated in a geometry which represents the real porous media with a high degree of accuracy. Navier-Stokes equations may be discretized using different approaches: the finite element method (FEM) (Lesueur *et al.*, 2017), the finite difference method (FDM) (Mostaghimi *et al.*, 2013; Ramandi *et al.*, 2017) and the finite volume method (FVM) (Pereira Nunes *et al.*, 2015; Starnoni *et al.*, 2017; Taylor *et al.*, 2017). Another approach, which is useful in porous media modelling, is the Lattice-Boltzmann method (LBM), which is based on a quasi-microscopic approach instead of the discretization of macroscopic continuum equations (Chen, Doolen, 1998). The LBM is used for modelling in rocks (Andrä *et al.*, 2013) as well as in soils (Baveye *et al.*, 2017).

The process of direct modelling based on CT imaging consists of the following steps: a CT scan, 3D image reconstruction, image processing, and binarization, pore space geometry reconstruction, the generation of a computational mesh, the simulation itself, and the post-processing of the simulation results. As yet, there is no single established workflow and most of these steps may be performed in multiple ways; however, each step requires optimization and may have an impact on the results of the simulation. Numerous studies have been presented, which estimate the impact of various aspects of direct modelling on the quality of 3D images and more particularly, their impact on the numerical calculation of hydraulic conductivity in porous materials. These aspects include, among others: CT reconstruction, noise reduction, changing the bit depth of the image (Houston *et al.*, 2013; Pot *et al.*, 2020; Schläuter *et al.*, 2014), and image segmentation (Baveye *et al.*, 2010; Gackiewicz *et al.*, 2019; Hapca *et al.*, 2013; Houston *et al.*, 2013; Iassonov *et al.*, 2009; Leu *et al.*, 2014; Schläuter *et al.*, 2014; Wang *et al.*, 2011). The estimated saturated water conductivity varied due to threshold errors of up to

32% for sandstone (Leu *et al.*, 2014) and for soils, the value found for one threshold was over 4 times higher than it was for another (Gackiewicz *et al.*, 2019). Also, the impact of the voxel resolution on the estimation of conductivity was investigated. Borujeni *et al.* (2013) evaluated numerous LBM and FEM grids generated for an artificial 3D image at different resolutions. A similar study, based on different modelling approaches, was presented by Shah *et al.* (2016) for sandstone permeability estimations; it used pore network modelling and the LBM. Variations in permeability have been demonstrated for four sandstone images of different sizes and resolutions (Bazaikin *et al.*, 2017; Borujeni *et al.*, 2013; Guan *et al.*, 2019; Shah *et al.*, 2016). Guan *et al.* (2019) investigated the impact of a decrease in image resolution (simulated by pixel binning) on estimates of permeability.

Despite the obvious impact of the resolution of the CT image, which is directly linked to the accuracy of pore space representations in permeability estimations, numerical mesh generation may also influence permeability estimation results. To date, this has not been investigated in the literature. Only one attempt has been made to explore this issue, in which a comparison of two mesh refinement levels were applied to the tomography image of only one sandstone sample (Guibert *et al.*, 2015). This study indicated that numerical mesh generation may be an important issue in the estimation of numerical permeability as the relative error of the permeability estimate decreased from 50% for the first refinement level to 15% for the second.

The aim of this study is to analyse the impact of the accuracy of the reproduction of the actual pore space by a numerical mesh on an SWC estimate with direct modelling. Understanding this relationship would help researchers to find the most relevant compromise between the computational complexity of a model and the accuracy of an estimate. For this reason, a simplified method of the estimation of error is proposed in this work. The study is based on an analysis of numerous samples with four different mesh refinement levels.

MATERIALS AND METHODS

Six samples were examined, which included four different fractions of sieved sand, and two sandstone cores. The sand used in the samples was obtained from the Vistula River near Puławy (Poland). The three samples (s1, s2, s3) contained sieved sand with grain sizes in the ranges of 0.08–0.16, 0.16–0.32, and 0.32–0.5mm, while the fourth (s4) contained sand sieved through a 0.5 mm sieve and additionally milled in a planetary mill (Pulverisette 6 classic line, Fritsch, Germany, Idar-Oberstein) for 10 minutes. The purpose of milling the sand was to increase the fine fraction content in the sample, leading to a more complicated pore geometry which is far more demanding with regard to X-ray CT analysis and modelling.

The particle size distribution (PSD) of the fourth sample was measured using the laser diffractometry method (LDM). A Malvern Mastersizer 2000 (Malvern Panalytical, Great Britain) with a measurement range of 0.02 μm to 2 mm was used to determine the PSD. In order to obtain homogeneity in the measured soil suspension, a Hydro G dispersion unit was used. The pump speed was set at 1750 rpm and the stirrer speed was 700 rpm. The light intensity, measured by detectors, was used to calculate the PSD according to the Mie theory (ISO 13320:2009, 2009). The Mie model parameters include an absorption coefficient of 0.1 and a refractive coefficient of 1.52 (Bieganski *et al.*, 2013). The PSD determined for sample s4 is as follows: clay (< 2 μm) 0.96%, silt (2-50 μm) 6.88% and sand (> 50 μm) 92.16%.

The sample material was poured into polypropylene tubes (4 mm i.d.) with low X-ray absorbance to a height of 10 mm. The sample was subsequently compacted using vibration.

In addition to the four sand samples, two sandstone samples (s5, s6) were also prepared. The fine-grained sandstone was collected from western Taiwan, Kueichulin Formation: Yutengping Sandstone (2 409 m depth) and Kuanyinshan Sandstone (2 531 m depth). There were two cubes (8x8x8 mm) of each sample.

Both sand and sandstone samples were scanned with an X-ray CT microtomograph (GENanotom180S) with a 180 kV/15 W microfocus X-ray tube. For each sample, two scans (a, b) were made. For the sand samples, two distinct regions of sand material – the first in the bottom part of the tube (a) and the second in the upper part (b) – were scanned. The sandstone samples were cut into two pieces from the collected cores and each was scanned independently. For each scan, a series of 1200 2D radiograms were collected, with the sample rotating 360° using a rotation step of 0.3°. Each 2D radiogram was averaged over 15 images for sand samples (20 images for sandstone samples) to reduce noise. The images were recorded using the detector, which has a resolution of 2284x2304 pixels registering images at the 14-bit gray-level depth. The X-ray source was operated at 90 kV with a 120 μA cathode current for sand samples (110 kV, 160 μA for sandstone) and a tungsten exit window. Immediately before each scan, a short pre-scan was made which lasted for 30 min to pre-heat the sample and minimize the impact of thermal expansion during the scan on the reconstructed 3D image. The voxel size obtained from these CT scans was 2 μm for sand samples and 2.28 μm for sandstone. Due to the nature of the sandstone samples, *e.g.* the larger diameter, there were differences in some of the CT scan parameters.

A tomographic reconstruction was performed on a series of radiograms using DatosX software (version 2.0.1, GE Sensing & Inspection Technologies GmbH, Germany).

The beam hardening correction was not necessary, although the exit window filter was not used during the X-ray scan. The received 3D volume was saved as a 16 bit TIFF image.

For further image processing, ImageJ (version 1.51k) software was used. Initially, the brightness of the images was adjusted. Following this, the images were saved in an 8-bit grayscale format to reduce the disk space and RAM needed for further processing. For further processing, a cylindrical region of interest (ROI) with a diameter of 4.2 mm and a height of 3.17 mm was chosen. The ROI was filtered twice using a median filter with a 3-pixelkernel size. The filtered images were then binarized. The binarization was performed using Ridler's iterative inter-means thresholding algorithm (Ridler, Calvard, 1978).

The total porosity (TP) and the specific surface area (SSA) were calculated based on the binarized images. To determine the porosity, the Volume Fraction function of the BoneJ plugin (version 1.4.2, open-source) for ImageJ was used. The total porosity was calculated as the ratio of the volume of voxels representing the pores to the total volume of the analysed image. The pore surface in a 3D image consists of rectangular voxel walls forming a castellated shape, which is significantly different from the actual pore surface of the scanned objects, which has an irregular shape. The marching cubes algorithm (Ridler, Calvard, 1978), which converts the set of voxels into a triangle mesh, was used to reproduce the surface of the pores. For this purpose, the Isosurface function was used in the BoneJ plugin with the "resampling" parameter set to 2, to determine the surface area of the pore-solid boundary. Dividing this surface area by the total sample volume gives the SSA. The triangulated representation of the pore space boundary surface was saved in a stereolithography (STL) file format for further processing in the computational mesh generation procedure. The image-based total porosities and specific surface areas were then compared to the same characteristics determined for the generated meshes.

For each sample, four computational grids that reflected the real pore geometry with increasing degrees of accuracy were generated based on the same pore space STL representation received from the CT. The parameter that varied between the grids for each sample was the number of initial cells, which determined the minimum size of the numeric grid cell. For each 3D image, meshes were constructed using the initial background grids with 10x10x10 (hereinafter referred to as m10), 20x20x20 (m20), 30x30x30 (m30) and 40x40x40 (m40) of initial cells (Fig. 1).

As the grid cells are refined five times in the neighbourhood of the pore surface, the size of the initial cells directly affects the complexity and accuracy of the mapping of the pore space of the final computational grid (Table 1). The greater the number of initial cells, the greater the final number of cells of the mesh and the time required to generate them. Because all of the grids had the same cell

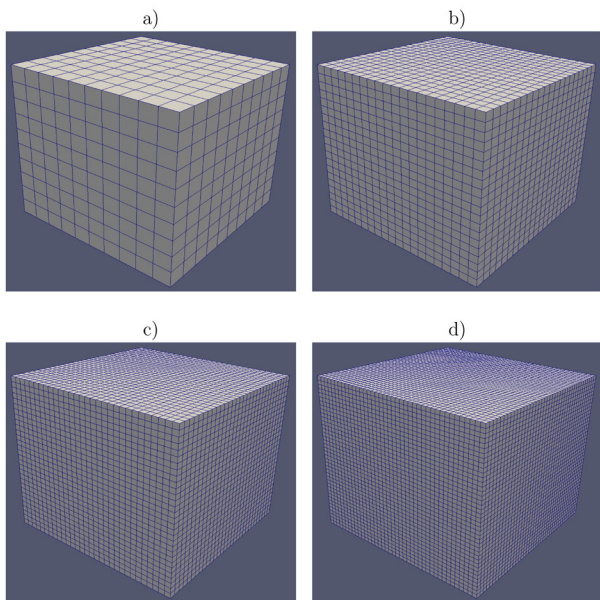


Fig. 1. Initial background grids of varying complexity (a – m10, b – m20, c – m30, d – m40).

Table 1. Size of initial cells and minimum size of cells in individual calculation grids

Calculation grid	Edge of initial cell (mm)	Minimum edge of final cell (μm)
m10	0.40	12.50
m20	0.20	6.25
m30	0.13	4.16
m40	0.10	3.12

division limit during their creation process, the smallest cells were in the most detailed grids with the largest number of initial cells.

In order to generate the computational grid, the STL triangulated surface of the pore space of the samples created earlier for the calculation of the specific surface area was used. All pre-processing, simulations, and postprocessing were conducted using the OpenFOAM computational fluid dynamics (CFD) package. The mesh was generated using the blockMesh and snappyHexMesh tools from this package. At the beginning, blockMesh generated an initial base grid that had the form of a cuboid consisting of 1000, 8000, 27000, or 64000 initial cells (m10, m20, m30, or m40). Subsequently, the computational grid was refined and adjusted to the shape of the pore geometry saved in the STL using snappyHexMesh.

Adjusting the original mesh to the desired shape defined by the pore surface consisted of several stages. Firstly, the initial background mesh cells were refined near the pore surface. In this study, the cells were refined up to five times. Then the cells which did not belong to the flow domain

defined by the pores were removed. At this stage, the mesh consisted solely of cuboids and was an approximated, castellated representation of the pore space (Fig. 2a). For the next step, cells that contained the pore surface were divided by that surface and the vertices of the cells were adjusted to follow the pore surface as closely as possible. The final stage of mesh generation was an iterative process of cell quality checks and shape adjustments based on mesh quality constraints. The flow domain represented by the mesh was the pore space determined by the CT of the sample, while the remainder of the sample, treated as a non-permeable solid body, was simply not included in the generated mesh. Finally, the mesh of the desired shape was created (Fig. 2b).

Despite the mesh quality constraints enforced during the mesh generation procedure, the quality of the final mesh had to be checked. The mesh was checked by the checkMesh program (part of the OpenFOAM package), which calculates the statistics of the mesh (number of elements, number of cells of individual types) and performs topology and geometry tests. As a part of the geometry tests, the parameters of the mesh elements were calculated, such as the proportions between the lengths of individual edges, or skewness. Cells with an overly high skewness value could have an adverse effect on the quality of the simulation and were removed. As the number removed did not exceed 0.003% of the total number of cells, it may be assumed that the impact of the deleted cells on the geometry of the whole image was negligible.

Numerical calculations were carried out using the simpleFoam program (OpenFOAM package), which solves the NS equations for incompressible steady-state flows with the finite volume method (FVM) based on the Semi-Implicit Method for Pressure Linked Equations (SIMPLE) algorithm. SIMPLE is an iterative algorithm that was first proposed by Patankar and Spalding (Patanekar *et al.*, 1972) for the numerical solution of the NS equations. As a result of these calculations, a discrete spatial distribution was obtained for the pressure p and velocity U of the liquid in the analysed area.

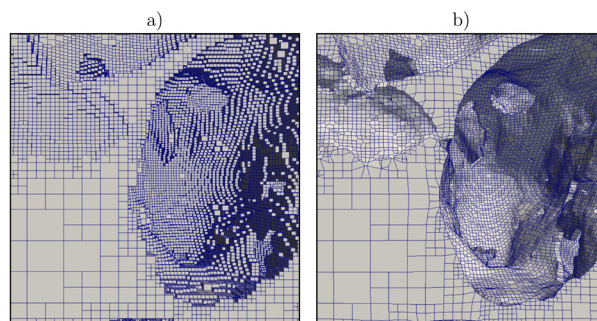


Fig. 2. Surface of the numerical grid: a) before and b) after smoothing.

The NS equations comprise the momentum balance (Eq. (1)) and the continuity (Eq. (2)), where: \bar{u} is a velocity vector (m s^{-1}), ρ is fluid density (kg m^{-3}), p is pressure ($\text{kg m}^{-1} \text{s}^{-2}$), μ is dynamic viscosity ($\text{kg m}^{-1} \text{s}^{-1}$) Navier-Stokes saturated conductivity, τ is a strain rate tensor (s^{-1}), \bar{F} are the external forces (kg m s^{-2}), and \bar{g} is the gravitational acceleration (m s^{-2}) (Eq. (3)):

$$u_j \frac{\partial}{\partial x_j} (\rho u_i) = -\frac{\partial p}{\partial x_i} + \mu \frac{\partial \tau_{ij}}{\partial x_j} + \bar{F}_i, \quad (1)$$

$$\frac{\partial}{\partial x_j} (\rho u_j) = 0, \quad (2)$$

$$\bar{F} = p \bar{g}. \quad (3)$$

The simulation requires appropriate boundary conditions. In the computational grid, the faces of the cells are assigned one out of a few types of usable patches, which have specific boundary conditions. Input and output patches are assigned to the surfaces at the inlet and outlet ends of the cylinder, respectively. The other patch, called the “sand_boundary”, represents the pore surface of the modelled medium. The initial and boundary conditions were determined for the dependent variables pressure p and speed U (Table 2). The value of the fluid velocity was fixed at 10^{-5} m s^{-1} , and the pressure was established at 0 Pa on the input patch with zero gradient Neuman conditions on the output patch. The input and output patches were equivalent to the top and bottom portions of the soil sample. No-slip boundary conditions were applied to the pore walls.

The water flow simulation mimics the constant head saturated conductivity measurement setup. Saturated water conductivity ($K_{sat}, \text{m s}^{-1}$), can be estimated based on information about the pressure difference ($\Delta p, \text{kg m}^{-1} \text{s}^{-2}$) between the input and output patches, the fluid velocity at the input patch ($U, \text{m s}^{-1}$) and the flow domain length ($\Delta l, \text{m}$):

$$K_{sat} = U \rho g \frac{\Delta l}{\Delta p}, \quad (4)$$

where: g is the gravitational constant (m s^{-2}) and ρ is the fluid density (kg m^{-3}).

Both the mesh generation and the subsequent calculations were executed in parallel using a message passing interface (MPI). For these calculations, a computing cluster

consisting of 7 nodes was used. Each node had 2 Intel Xeon E5-2690 processors, 256 GB RAM, and the operating system Centos 7.

The specific surfaces of the generated meshes were determined using custom software based on OpenFOAM and written for this purpose.

Numerical simulations simply generate a result for a given numerical mesh, model, and boundary conditions. The mesh quality is especially important for simulation results. Two factors of mesh quality must be considered. First, general numerical mesh quality factors like cell skewness, cell non-orthogonality, and the cell aspect ratio are taken into account during the mesh creation procedure and are usually not a problem. The second mesh quality factor is mesh precision, which may be understood as the accuracy of recovering the pore space geometry from the mesh. Unfortunately, the geometry of the pore media is naturally very complicated. This causes potential problems for mesh precision, in particular, problems with the correct meshing of the narrow areas of the pores.

A method to estimate the impact of mesh inaccuracy on simulation results is required. More particularly, for the problem of saturated conductivity estimation, the following method of error calculation based on observed geometrical mesh quality measurements is proposed. These geometrical mesh quality measures are the difference between the total porosity of the image and the grid and the difference between the specific surfaces of the image and the grid.

In order to estimate the error of the SWC calculation, the method proposed is based on the phenomenological Kozeny-Carman (KC) equation. The KC equation relates the SWC to the total porosity and the specific surface of the porous medium. The KC equation was used in the following equation from Kuang *et al.* (2011):

$$K_{sat} = \frac{\phi^3}{C_0 \tau^2 (1-\phi^2) \sigma^2} \frac{\rho g}{\mu}, \quad (5)$$

where: C_0 is the Kozeny constant, τ is the tortuosity (-), ρ is the liquid density (kg m^{-3}), μ is the dynamic viscosity of the liquid ($\text{kg m}^{-1} \text{s}^{-1}$), and g is the gravitational acceleration (m s^{-2}).

Table 2. Boundary and initial conditions (U_x , U_y , U_z -x-th, y-th and z-th components of U , U_n -velocity component normal to the output patch)

Variable	Initial conditions	Boundary conditions		
		patch “input”	patch “output”	patch “sand_boundary”
p	$p = 0$	$\nabla p = 0$	$p = 0$	$\nabla p = 0$
U	$U_x = 0$ $U_y = 0$ $U_z = 3 \times 10^{-5}$	$U_x = 0$ $U_y = 0$ $U_z = 1 \times 10^{-5}$	$\nabla U_n = 0$	$U = 0$

The margin of error in the estimation of the SWC from the KC equation may be calculated using the total derivative method. The independent variables that have the potential to contribute to the error in estimating the hydraulic conductivity in the KC equation are total porosity and the specific surface area. It may be assumed that the error in estimating the hydraulic conductivity ΔK will correspond to the sum of the error related to the uncertainty of porosity determination, $\Delta K_{KC}(\phi_0) = \left| \frac{\partial K_{KC}}{\partial \phi} \right|_{\phi_0} \Delta \phi$, and the error related

to the uncertainty of specific surface determination, $\Delta K_{KC}(\sigma_0) = \left| \frac{\partial K_{KC}}{\partial \sigma} \right|_{\sigma_0} \Delta \sigma$.

The equation for the error related to the uncertainty of the porosity measurement is:

$$\Delta K_{KC}(\phi_0) = \left| \frac{\phi^2}{c_0 \tau^2 (1-\phi^2) \sigma^2} \left(3 + \frac{2\phi^2}{1-\phi^2} \right) \frac{\rho g}{\mu} \right|_{\phi_0} \Delta \phi, \quad (6)$$

and may be written in the form:

$$\Delta K_{KC}(\phi_0) = K_{KC}(\phi_0) \left| \frac{3-\phi^2}{\phi(1-\phi^2)} \right|_{\phi_0} \Delta \phi. \quad (7)$$

The equation for the error related to the uncertainty of the specific surface measurement is:

$$\Delta K_{KC}(\sigma_0) = \left| \frac{\phi^2}{c_0 \tau^2 (1-\phi^2) \sigma^2} \left(-\frac{2}{\sigma} \right) \frac{\rho g}{\mu} \right|_{\sigma_0} \Delta \sigma, \quad (8)$$

and may be simplified to:

$$\Delta K_{KC}(\sigma_0) = K_{KC}(\sigma_0) \left| -\frac{2}{\sigma} \right|_{\sigma_0} \Delta \sigma. \quad (9)$$

Therefore, the relative error in the estimation of the SWC coefficient based on the KC equation (taking into account the uncertainty of the porosity and the specific surface measurement) may be written as:

$$\frac{\Delta K_{KC}}{K_{KC}}(\phi_0, \sigma_0) = \left| \frac{3-\phi^2}{\phi(1-\phi^2)} \right|_{\phi_0} \Delta \phi + \left| \frac{-2}{\sigma} \right|_{\sigma_0} \Delta \sigma. \quad (10)$$

The value of the total porosity error, $\Delta \phi$, was assumed to be the difference between the total porosity calculated from the grid and the total porosity calculated from the binarized image. The specific surface error $\Delta \sigma$ was determined analogously.

RESULTS AND DISCUSSION

The finest meshes, m20, m30, and m40, were successfully generated for all samples. But the coarsest mesh, m10, was only successfully generated for the sand samples (s1, s2, s3, s4). It was not possible to generate the coarse mesh for the sandstone samples (s5, s6). This was due to the narrow pore throats in the sandstone material, which did not allow for mesh cell generation with the minimum allow-

able mesh size of m10 (Table 1). A prerequisite for creating the mesh is an adequate connection between the top and the bottom of the pore network. In the tomographic image under consideration, when such a connection had a diameter smaller than the minimum edge of the finer cells (Table 1), the creation of the grid was not possible (Fig. 3).

The final computational mesh complexity, which may be understood as the number of cells in the mesh, is an important factor for the practical application of the mesh. The greater the number of cells that were in the initial background grid, the greater the number of mesh cells that were observed in the final mesh (Fig. 4). The number of cells in a mesh generated for a given sample was very different depending on whether they were the finest (m40) and the coarsest (m10) meshes, reaching a ratio equal to 30 in the case of sample s4. Lower values of this ratio of ~10 were observed for samples s1a and s1b. In general, the higher the value of the SSA of the pores in the sample, the greater the differences in mesh complexity between the m10, m20, m30, and m40 meshes. This dependence may be easily explained by taking into account that during the mesh

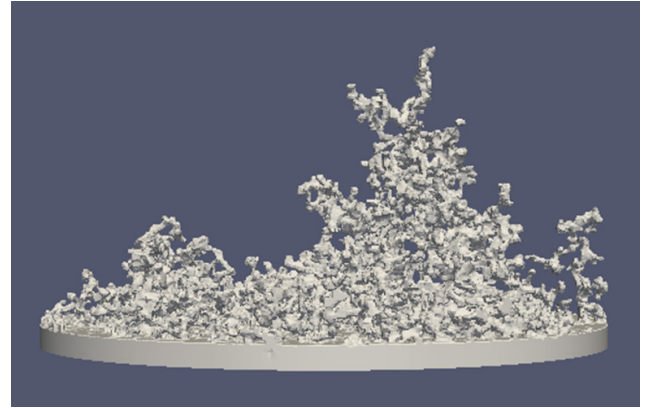


Fig. 3. Partially created mesh, where generation failed due to pore throats too narrow in comparison with the size of the finest possible mesh cell.

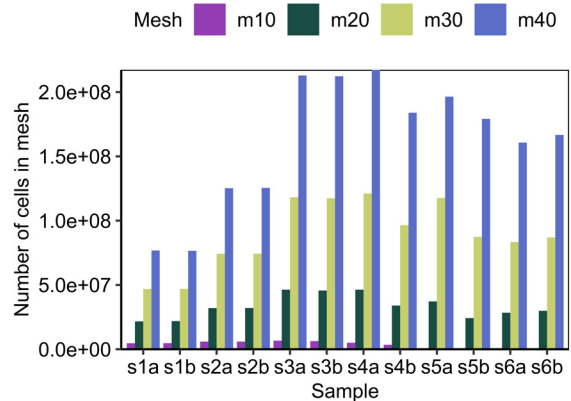


Fig. 4. Number of cells in meshes of varying degrees of detail generated from tomographic images.

generation procedure, the initial cells are refined 5 times in the direct neighbourhood of the pore surface, and these cells are as small as possible. The greater the distance from the pore surface, the lower the refinement level and if the distance is high enough, the cells of the initial background cell may not even be refined at all.

The time required for mesh generation was related to the complexity of the mesh. The time required for mesh generation for a given sample was also dependent on the initial background grid (Fig. 5). Based on the 44 grids created, it may be observed that the relationship between the number of cells in the final mesh and the time taken to generate it is close to linear (Fig. 6).

Meshes generated in different ways but representing the same pore medium varied widely in complexity. For practical reasons the mesh chosen for each simulation is a trade-off between the resources required for mesh generation and simulation, and the accuracy of the simulation

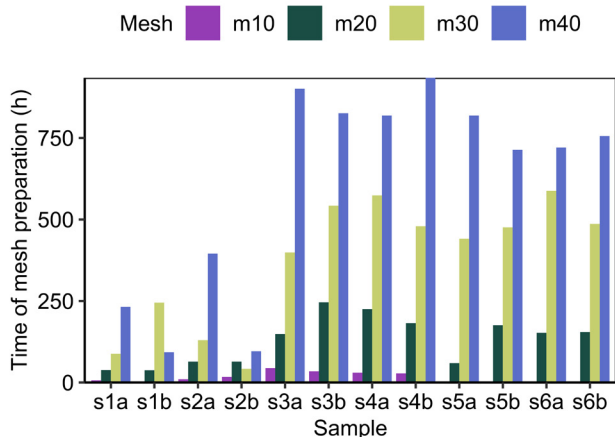


Fig. 5. Mesh generation time for meshes of varying degrees of detail generated from tomographic images.

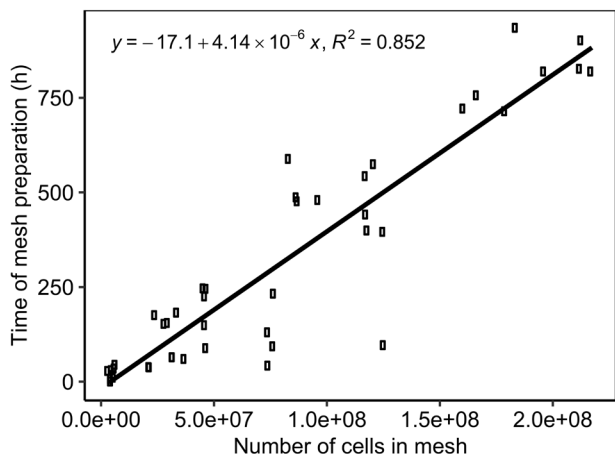


Fig. 6. Time required to generate meshes as a function of the number of cells in the generated meshes.

results. The prerequisite for a good quality mesh is accurate pore geometry representation. Two factors may be used to quantify mesh quality, the differences between mesh and pore medium: SSA and TP. In an ideal case, exactly the same geometry of pore space as that represented in the mesh as in the CT image of an examined pore medium would be achieved, and no differences in SSA or TP would be observed. But in practice, the geometry of the pore medium as reflected by the mesh differs slightly from the real sample. This is due to problems with meshing the narrow regions of the pores, where the dimensions of the pores are smaller than the smallest possible cell permitted by the mesh generation procedure.

Figure 7 shows sample cross-sections for increasing levels of mesh complexity (m10, m20, m30, and m40) for sample s1a. Meshes with a bigger initial cell size (m10) do not fill the pore space well, which is visible in the small spaces between grains of sand. For the m10 mesh, this is very easily observable between most grains. For the m20 mesh, these areas still occur frequently but are much smaller compared to the m10 version. For the m30 mesh, they are almost absent – they are only observed in two areas in the cross-section shown. The m40 grid appears to reproduce the pore space exactly.

In order to quantify the quality of the pore geometry representation, the values of the SSAs and TPs calculated for each of the resulting meshes were compared with their counterparts determined from the CT images of the porous media, which were treated as reference values. It may be noted that the SSAs of the computational grids are lower than the SSAs of the binarized CT images, and the greater the accuracy of the grid, the higher the specific surface value (Fig. 8 and 9).

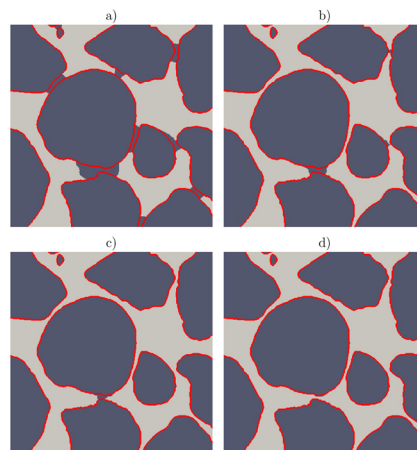


Fig. 7. Example of the cross-section through calculated grids: a) m10, b) m20, c) m30, d) m40. Colour: beige – the area where the mesh was created is marked, red – the space separating the pores from the solid phase (based on a tomographic scan), dark gray – the space treated by the mesh as grains.

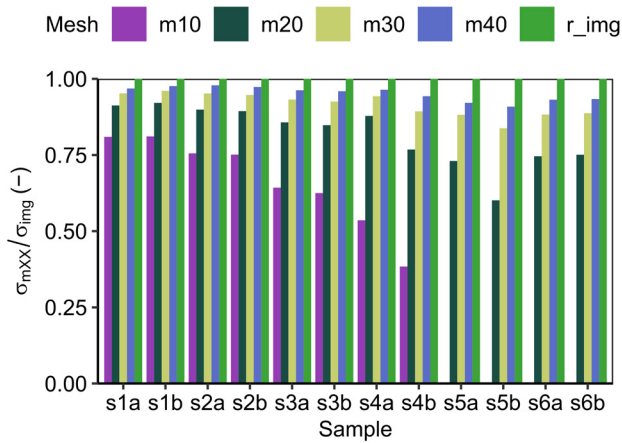


Fig. 8. Specific surface areas of computational grids (m10, m20, m30, m40) normalized to the value of the specific surface of the binarized image (ref_img).

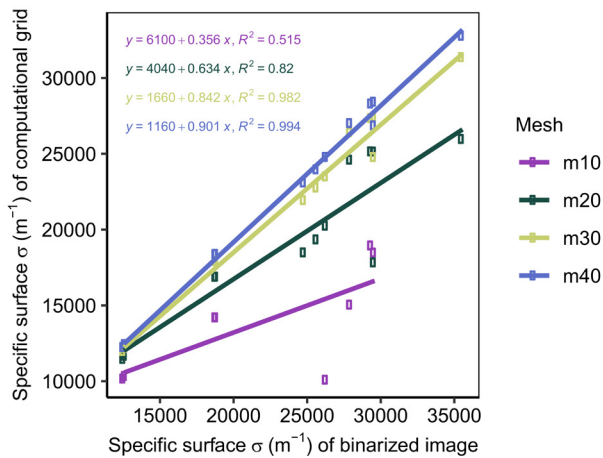


Fig. 9. Specific surface areas of the computational grids as a function of the specific surface area of binarized images.

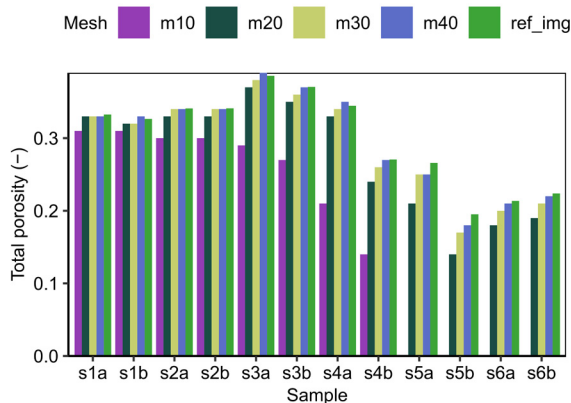


Fig. 10. Total porosity of the computational grids (m10, m20, m30, m40) and the corresponding binarized image (ref_img).

The TPs of the computational grids are usually lower than the TPs of the images (Fig. 10); however, the relationship between greater mesh accuracy and higher porosity of the mesh (Fig. 11) is not as clearly apparent as in the case of the SSA.

The grids created were used to simulate saturated flow in a pore medium. Based on the fluid velocity and the pressure values of the input and output patches, the coefficients of saturated water conductivity, K_{sat} , were calculated for each calculation grid and then compared with other grids (Fig. 12). The estimated values of the saturated conductivities determined for the finest m40 meshes were treated as reference values.

The estimated error values ΔK_{sat} are shown in Table 3. An evaluation method for the evaluation of the error of estimation of the SWC based on an analysis of the KC equation was proposed. The development of the proposed error estimation method is formally correct, although it is based on the assumption of the correctness of the KC equation which may be disputed in the context of specific pore media. It is important to note that the proposed method for SWC error

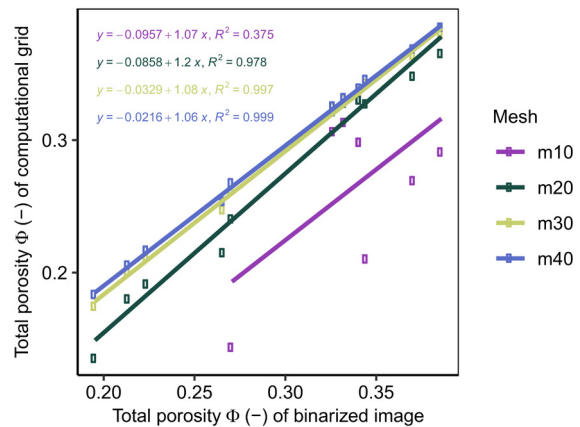


Fig. 11. Total porosity of the computational grids as a function of the total porosity of the binarized images.

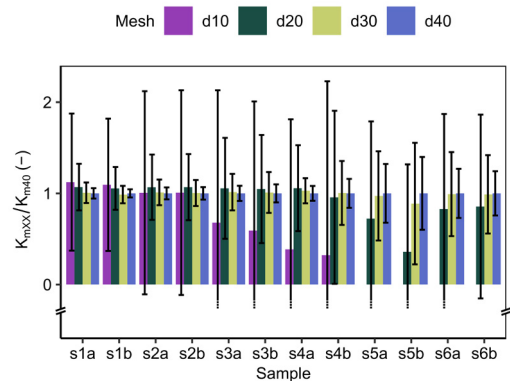


Fig. 12. Values of simulated SWC for different grids normalized for the value of saturated conductivity simulated for the finest m40 grid.

Table 3. Values of the numerically estimated SWC coefficient together with their errors (calculated based on equation 10), the root mean square value of the RMSE error calculated from a comparison of the series of K_{sat} coefficients for the m10, m20, and m30 grids with the values of K_{sat} for the m40 grid

Mesh	m10		m20		m30		m40	
Sample	K_{sat} (ms ⁻¹)	ΔK_{sat} (ms ⁻¹)	K_{sat} (ms ⁻¹)	ΔK_{sat} (ms ⁻¹)	K_{sat} (ms ⁻¹)	ΔK_{sat} (ms ⁻¹)	K_{sat} (ms ⁻¹)	ΔK_{sat} (ms ⁻¹)
s1a	5.60×10^{-4}	3.75×10^{-4}	5.33×10^{-4}	1.27×10^{-4}	5.02×10^{-4}	5.62×10^{-5}	4.98×10^{-4}	2.83×10^{-5}
s1b	5.06×10^{-4}	3.36×10^{-4}	4.88×10^{-4}	1.08×10^{-4}	4.57×10^{-4}	4.42×10^{-5}	4.63×10^{-4}	2.08×10^{-5}
s2a	2.23×10^{-4}	2.47×10^{-4}	2.37×10^{-4}	7.94×10^{-5}	2.24×10^{-4}	3.12×10^{-5}	2.22×10^{-4}	1.46×10^{-5}
s2b	2.25×10^{-4}	2.50×10^{-4}	2.38×10^{-4}	8.09×10^{-5}	2.24×10^{-4}	3.19×10^{-5}	2.23×10^{-4}	1.53×10^{-5}
s3a	9.01×10^{-5}	1.93×10^{-4}	1.40×10^{-4}	7.36×10^{-5}	1.35×10^{-4}	2.66×10^{-5}	1.33×10^{-4}	1.11×10^{-5}
s3b	6.85×10^{-5}	1.64×10^{-4}	1.21×10^{-4}	6.86×10^{-5}	1.17×10^{-4}	2.59×10^{-5}	1.16×10^{-4}	1.15×10^{-5}
s4a	3.97×10^{-5}	1.47×10^{-4}	1.09×10^{-4}	4.85×10^{-5}	1.06×10^{-4}	1.42×10^{-5}	1.03×10^{-4}	8.36×10^{-6}
s4b	1.81×10^{-5}	1.07×10^{-4}	5.37×10^{-5}	5.33×10^{-5}	5.64×10^{-5}	1.97×10^{-5}	5.61×10^{-5}	8.91×10^{-6}
s5a	–	–	1.12×10^{-5}	1.65×10^{-5}	1.50×10^{-5}	7.57×10^{-6}	1.55×10^{-5}	4.98×10^{-6}
s5b	–	–	1.44×10^{-6}	3.85×10^{-6}	3.56×10^{-6}	2.67×10^{-6}	4.01×10^{-6}	1.60×10^{-6}
s6a	–	–	1.17×10^{-5}	1.47×10^{-5}	1.40×10^{-5}	6.49×10^{-6}	1.41×10^{-5}	3.80×10^{-6}
s6b	–	–	1.42×10^{-5}	1.67×10^{-5}	1.64×10^{-5}	7.12×10^{-6}	1.66×10^{-5}	4.02×10^{-6}
RMSE (ms ⁻¹)	4.35×10^{-5}		1.42×10^{-5}		2.42×10^{-6}		–	

estimation may be applied to any CFD approach of SWC modelling based on CT pore media images. The only input parameters of this method are easily determined; the SSA and the TP of the numerical mesh as well as the CT image of the pore medium.

As Table 3 and Fig. 12 show, the proposed method for determining the errors in the numerical assessment of hydraulic conductivity seems to work well. While the SWC value estimated for the m40 grid, may be considered as optimal, it is significantly different from the SWC values estimated for other grids, it always remains in the range determined by the error bars of SWC estimated for less accurate grids. In addition, for all of the samples studied, the absolute value of the error monotonically decreases as the mesh more accurately reproduces the pore space, in the following order: m10→ m20→m30→m40. The root mean square values of the saturation coefficient error are also presented in Table 3, where the reference value is the series of conductivity coefficients for the m40 grid.

Histograms of the fluid velocities were calculated from the distribution of velocities in each set of computational cells. From a sample histogram for sample s2a, in Fig. 13 one may observe significantly fewer cells at the lowest speeds for the grid with the lowest accuracy of mapping the pore network.

In the mesh of lower accuracy, there are few locations with a velocity value significantly higher than average, while in the more accurate mesh, the distribution of velocities is more homogenous. These findings are congruent

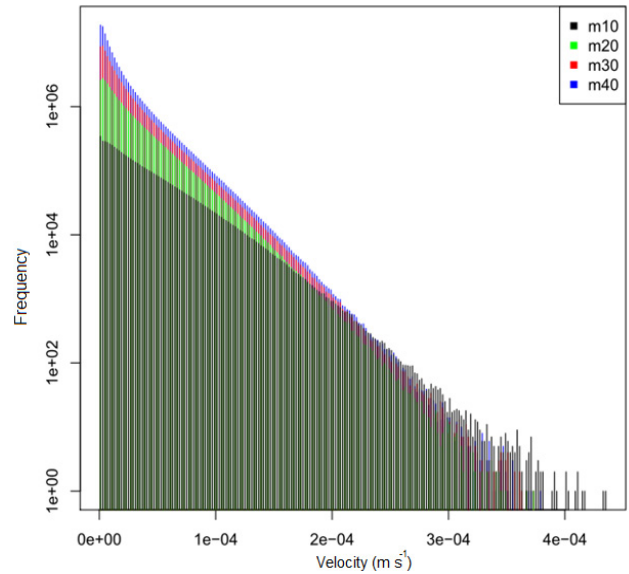


Fig. 13. Histogram of velocities in calculation cells for sample s2a.

with the histogram (Fig. 13) – the more ways water can flow through the sample, the lower the values of the flow are in specific points within it.

CONCLUSIONS

1. The more detailed the mesh is, the more accurate the results of the simulations are. Mesh precision is especially important for modelling processes in complex geometries,

such as in porous media. For practical reasons related to computational complexity and available resources, there is always a trade-off between mesh precision and simulation accuracy. In the case of numerical estimations of the saturated conductivity of porous media, based on the cases analysed, the following recommendation is made: the minimum size of the cell in the meshes used for simulations has to be no more than two times the size of the voxel used in tomographic scans of the pore medium.

2. The proposed method for calculating the error of the estimation for the value of the saturated water conductivity was based on the global numerical mesh geometry characteristics: the specific surface area and the total porosity give reasonable error estimates. However, due to the arbitrary assumptions made in the method, an additional method of validation for the proposed approach should be considered in future studies.

3. If the initial background mesh from which the final computational grid is built is too coarse, the quality of the simulations is negatively affected. In terms of simulation quality, the degree of tolerance to grid precision is very low. The two finest meshes (m40 and m30) produced reasonable results, while the third mesh (m20) produced erroneous results. In the case of the coarsest mesh (m10), the simulation results were unacceptable, and for some samples, it was not even possible to create the correct grid.

Conflict of interest: The authors declare no conflict of interest.

REFERENCES

- Andrä H., Combaret N., Dvorkin J., Glatt E., Han J., Kabel M., Keehm Y., Krzikalla F., Lee M., Madonna C., Marsh M., Mukerji T., Saenger E.H., Sain R., Saxena N., Ricker S., Wiegmann A., and Zhan X., 2013.** Digital rock physics benchmarks-part II: Computing effective properties. *Comput. Geosci.*, 50, 33-43. <https://doi.org/10.1016/j.cageo.2012.09.008>
- Baveye P.C., Laba M., Otten W., Bouckaert L., Dello Sterpaio P., Goswami R.R., Grinev D., Houston A., Hu Y., Liu J., Mooney S., Pajor R., Sleutel S., Tarquis A., Wang W., Wei Q., and Sezgin M., 2010.** Observer-dependent variability of the thresholding step in the quantitative analysis of soil images and X-ray microtomography data. *Geoderma*, 157, 51-63. <https://doi.org/10.1016/J.GEODERMA.2010.03.015>
- Baveye P.C., Pot V., and Garnier P., 2017.** Accounting for sub-resolution pores in models of water and solute transport in soils based on computed tomography images: Are we there yet? *J. Hydrol.*, 555, 253-256. <https://doi.org/10.1016/J.JHYDROL.2017.10.021>
- Bazaikin Y., Gurevich B., Iglauer S., Khachkova T., Kolyukhin D., Lebedev M., Lisitsa V., Reshetova G., 2017.** Effect of CT image size and resolution on the accuracy of rock property estimates. *J. Geophys. Res. Solid Earth*, 122, 3635-3647. <https://doi.org/10.1002/2016JB013575>
- Bieganowski A., Chojecki T., Ryżak M., Sochan A., and Lamorski K., 2013.** Methodological Aspects of Fractal Dimension Estimation on the Basis of Particle Size Distribution. *Vadose Zo. J.*, 12, 0. <https://doi.org/10.2136/vzj2012.0064>
- Borujeni A.T., Lane N.M., Thompson K., and Tyagi M., 2013.** Effects of image resolution and numerical resolution on computed permeability of consolidated packing using LB and FEM pore-scale simulations. *Comput. Fluids*, 88, 753-763. <https://doi.org/10.1016/j.compfluid.2013.05.019>
- Chen S. and Doolen G.D., 1998.** Lattice Boltzmann method for fluid flows. *Ann. Rev. Fluid Mech.*, 30, 329-364. <https://doi.org/10.1146/annurev.fluid.30.1.329>
- Chen S., Yang B., and Zheng C., 2017.** A lattice Boltzmann model for heat transfer in porous media. *Int. J. Heat Mass Transf.*, 111, 1019-1022. <https://doi.org/10.1016/j.ijheatmasstransfer.2017.04.054>
- Dal Ferro N., Strozzi A.G., Duwig C., Delmas P., Charrier P., and Morari F., 2015.** Application of smoothed particle hydrodynamics (SPH) and pore morphologic model to predict saturated water conductivity from X-ray CT imaging in a silty loam Cambisol. *Geoderma*, 255-256, 27-34. <https://doi.org/10.1016/j.geoderma.2015.04.019>
- Gackiewicz B., Lamorski K., and Sławiński C., 2019.** Saturated water conductivity estimation based on X-ray CT images – evaluation of the impact of thresholding errors. *Int. Agrophys.*, 33, 49-60. <https://doi.org/10.31545/intagr/104376>
- Guan K.M., Nazarova M., Guo B., Tchelep H., Kovscek A.R., and Creux P., 2019.** Effects of image resolution on sandstone porosity and permeability as obtained from X-Ray microscopy. *Transp. Porous Media*, 127, 233-245. <https://doi.org/10.1007/s11242-018-1189-9>
- Guibert R., Nazarova M., Horgue P., Hamon G., Creux P., and Debenest G., 2015.** Computational permeability determination from pore-scale imaging: Sample Size, Mesh and Method Sensitivities. *Transp. Porous Media*, 107, 641-656. <https://doi.org/10.1007/s11242-015-0458-0>
- Hapca S.M., Houston A.N., Otten W., and Baveye P.C., 2013.** New local thresholding method for soil images by minimizing grayscale intra-class variance. *Vadose Zo. J.*, 12, 1-13. <https://doi.org/10.2136/vzj2012.0172>
- Horgue P., Soulaire C., Franc J., Guibert R., and Debenest G., 2015.** An open-source toolbox for multiphase flow in porous media. *Comput. Phys. Commun.*, 187, 217-226. <https://doi.org/10.1016/j.cpc.2014.10.005>
- Houston A.N., Schmidt S., Tarquis A.M., Otten W., Baveye P.C., and Hapca S.M., 2013.** Effect of scanning and image reconstruction settings in X-ray computed microtomography on quality and segmentation of 3D soil images. *Geoderma*, 207-208, 154-165. <https://doi.org/10.1016/J.GEODERMA.2013.05.017>
- Iassonov P., Gebrenegus T., and Tuller M., 2009.** Segmentation of X-ray computed tomography images of porous materials: A crucial step for characterization and quantitative analysis of pore structures. *Water Resour. Res.*, 45. <https://doi.org/10.1029/2009WR008087>
- Jarvis N.J., 2007.** A review of non-equilibrium water flow and solute transport in soil macropores: principles, controlling factors and consequences for water quality. *Eur. J. Soil Sci.*, 58, 523-546. <https://doi.org/10.1111/j.1365-2389.2007.00915.x>

- Khan F., Enzmann F., Kersten M., Wiegmann A., and Steiner K., 2012.** 3D simulation of the permeability tensor in a soil aggregate on basis of nanotomographic imaging and LBE solver. *J. Soils Sediments*, 12, 86-96. <https://doi.org/10.1007/s11368-011-0435-3>
- Kuang X., Sansalone J., Ying G., and Ranieri V., 2011.** Pore-structure models of hydraulic conductivity for permeable pavement. *J. Hydrol.*, 399, 148-157. <https://doi.org/10.1016/j.jhydrol.2010.11.024>
- Larsbo M., Koestel J., and Jarvis N., 2014.** Relations between macropore network characteristics and the degree of preferential solute transport. *Hydrol. Earth Syst. Sci.*, 18, 5255-5269. <https://doi.org/10.5194/hess-18-5255-2014>
- Lesueur M., Casadiego M.C., Veveakis M., and Poulet T., 2017.** Modelling fluid-microstructure interaction on elasto-visco-plastic digital rocks. *Geomech. Energy Environ.*, 12, 1-13. <https://doi.org/10.1016/j.gete.2017.08.001>
- Leu L., Berg S., Enzmann F., Armstrong R.T., and Kersten M., 2014.** Fast X-ray Micro-Tomography of Multiphase Flow in Berea Sandstone: A Sensitivity Study on Image Processing. *Transp. Porous Media*, 105, 451-469. <https://doi.org/10.1007/s11242-014-0378-4>
- Mostaghimi P., Blunt M.J., and Bijeljic B., 2013.** Computations of absolute permeability on micro-CT images. *Math. Geosci.*, 45, 103-125. <https://doi.org/10.1007/s11004-012-9431-4>
- Patankar S. V., Spalding D.B., and Road E., 1972.** A calculation procedure for heat, mass and momentum transfer in three-dimensional parabolic flows. *Int. J. Heat Mass Transf.*, 15, 1787-1806.
- Pereira Nunes J.P., Bijeljic B., and Blunt M.J., 2015.** Time-of-flight distributions and breakthrough curves in heterogeneous porous media using a pore-scale streamline tracing algorithm. *Transp. Porous Media* 109, 317-336. <https://doi.org/10.1007/s11242-015-0520-y>
- Pot V., Zhong X., and Baveye P.C., 2020.** Effect of resolution, reconstruction settings, and segmentation methods on the numerical calculation of saturated soil hydraulic conductivity from 3D computed tomography images. *Geoderma*, 362, 114089. <https://doi.org/10.1016/j.geoderma.2019.114089>
- Ramandi H.L., Mostaghimi P., and Armstrong R.T., 2017.** Digital rock analysis for accurate prediction of fractured media permeability. *J. Hydrol.*, 554, 817-826. <https://doi.org/10.1016/J.JHYDROL.2016.08.029>
- Ridler T.W. and Calvard S., 1978.** Picture thresholding using an iterative selection method. *IEEE Trans. Syst. Man Cybern.*, 8, 630-632. <https://doi.org/10.1109/TSMC.1978.4310039>
- Schläuter S., Sheppard A., Brown K., and Wildenschild D., 2014.** Image processing of multiphase images obtained via X-ray microtomography: A review. *Water Resour. Res.*, 50, 3615-3639. <https://doi.org/10.1002/2014WR015256>. Received
- Shah S.M., Gray F., Crawshaw J.P., and Boek E.S., 2016.** Micro-computed tomography pore-scale study of flow in porous media: Effect of voxel resolution. *Adv. Water Resour.*, 95, 276-287. <https://doi.org/10.1016/j.advwatres.2015.07.012>
- Starnoni M., Pokrajac D., and Neilson J.E., 2017.** Computation of fluid flow and pore-space properties estimation on micro-CT images of rock samples. *Comput. Geosci.*, 106, 118-129. <https://doi.org/10.1016/j.cageo.2017.06.009>
- Taylor H.F., O'Sullivan C., Sim W.W., and Carr S.J., 2017.** Sub-particle-scale investigation of seepage in sands. *Soils Found.*, 57, 439-452. <https://doi.org/10.1016/J.SANDEF.2017.05.010>
- Wang W., Kravchenko A.N., Smucker A.J.M., and Rivers M.L., 2011.** Comparison of image segmentation methods in simulated 2D and 3D microtomographic images of soil aggregates. *Geoderma*, 162, 231-241. <https://doi.org/10.1016/J.GEODERMA.2011.01.006>
- Zuo L., Ajo-Franklin J.B., Voltolini M., Geller J.T., and Benson S.M., 2017.** Pore-scale multiphase flow modeling and imaging of CO₂ exsolution in Sandstone. *J. Pet. Sci. Eng.* 155, 63-77. <https://doi.org/10.1016/J.PETROL.2016.10.011>